



Rational design of mixed ionic and electronic conducting perovskite oxides for solid oxide fuel cell anode materials: A case study for doped SrTiO_3

Suwit Suthirakun ^a, Guoliang Xiao ^b, Salai Cheettu Ammal ^a, Fanglin Chen ^b, Hans-Conrad zur Loyer ^c, Andreas Heyden ^{a,*}

^a Department of Chemical Engineering, University of South Carolina, 301 S. Main St., Columbia, SC 29208, USA

^b Department of Mechanical Engineering, University of South Carolina, 300 Main St., Columbia, SC 29208, USA

^c Department of Chemistry and Biochemistry, University of South Carolina, 631 Sumter Street, Columbia, SC 29208, USA



HIGHLIGHTS

- Mixed p- and n-type doping leads to mixed ionic and electronic conductivity.
- Mixed p- and n-type doping strategy independent of doping site.
- p-Type doping at A-site in n-doped SrTiO_3 leads to highest conductivity.
- Computational predictions experimentally validated.

ARTICLE INFO

Article history:

Received 1 April 2013

Received in revised form

24 June 2013

Accepted 8 July 2013

Available online 17 July 2013

Keywords:

Mixed ionic/electronic conductivity

Doped SrTiO_3

Density functional theory

Solid oxide fuel cell anode

ABSTRACT

The effect of p- and n-type dopants on ionic and electronic conductivity of SrTiO_3 based perovskites were investigated both computationally and experimentally. Specifically, we performed density functional theory (DFT) calculations of Na- and La-doped SrTiO_3 and Na- and Nb-doped SrTiO_3 systems. Constrained *ab initio* thermodynamic calculations were used to evaluate the phase stability and reducibility of doped SrTiO_3 under both oxidizing and reducing synthesis conditions, as well as under anodic solid oxide fuel cell (SOFC) conditions. The density of states (DOS) of these materials was analyzed to study the effects of p- and n-doping on the electronic conductivity. Furthermore, Na- and La-doped SrTiO_3 and Na- and Nb-doped SrTiO_3 samples were experimentally prepared and the conductivity was measured to confirm our computational predictions. The experimental observations are in very good agreement with the theoretical predictions that doping n-doped SrTiO_3 with small amounts of p-type dopants promotes both the ionic and electronic conductivity of the material. This doping strategy is valid independent of p- and n-doping site and permits the synthesis of perovskite based mixed ionic/electronic conductors.

© 2013 Elsevier B.V. All rights reserved.

1. Introduction

Solid oxide fuel cells (SOFCs) are energy conversion devices with very high energy efficiency and low pollution for converting the chemical energy of fuels into electricity. A variety of feed gases can be used as fuels in SOFCs since they operate at high temperatures, promoting rapid reaction kinetics and allowing for internal reforming of hydrocarbon fuels or direct oxidation at the surface of the anode electrode. Most SOFC development has been focused on

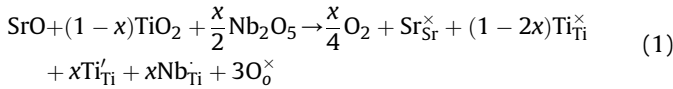
Ni-based cermet anodes due to their high electrical conductivity, excellent catalytic activity and current collectability, and robust mechanical properties. However, these anodes suffer from several limitations such as instability upon redox cycling [1], nickel coarsening [2–4], sulfur poisoning [5], and carbon deposition [6]. Hence, finding alternative anode materials to replace conventional Ni-based cermet electrodes has become a critical aim in developing SOFC technology. Since the Ni metal in Ni-based electrodes is the component that exhibits instability and low tolerance to sulfur impurities and coking, it has been suggested to remove the Ni metal and use only ceramic components for electron transport and fuel oxidation [7]. Furthermore, to maximize the electrochemically active surface area for fuel oxidation, the anode electrode should

* Corresponding author.

E-mail addresses: HEYDEN@cec.sc.edu, heyden.andreas@gmail.com (A. Heyden).

consist of only mixed ionic/electronic conducting materials. Among the ceramic anode materials, perovskite based oxides (ABO_3) are of great interest because they can accommodate various dopants and incorporate cations with multiple oxidation states, which permits tuning the electro-catalytic activity and provides a mechanism for tailoring electronic and ionic conductivity [8]. In addition, perovskite oxides have been shown to satisfy most intrinsic SOFC anode requirements such as high thermodynamic stability under anodic conditions [9–15] and strong resistance to carbon deposition [6,9,16,17] and sulfur poisoning [18–20].

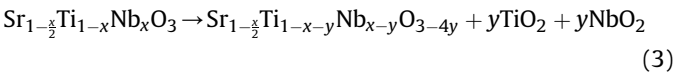
Over the past few years, several doping strategies to improve mixed ionic/electronic conductivity in perovskite oxides have been suggested. For example, Xiao et al. [21] and Neagu and Irvine [8] reported the stability and mixed ionic/electronic conductivity of mixed p- and n-doped SrTiO_3 . To better understand the functions of these dopants, we performed density functional theory (DFT) calculations to investigate the effects of p- and n-type dopants on the electronic conductivity and reducibility of SrTiO_3 based perovskites. The computational results confirmed that mixed p- and n-doping is an efficient strategy to obtain mixed ionic/electronic conductivity in perovskite oxides [22,23]. We find that the role of n-type dopants is to improve the electronic conductivity of the material by generating extra charges in the host lattice. At low oxygen chemical potentials typical of SOFC anodes the formal charge of the n-type dopants are electronically compensated by creating conduction electrons that hop via oxygen bridges from Ti^{3+} to Ti^{4+} cations. For example, substitution of Ti atoms in stoichiometric SrTiO_3 with Nb (n-type) atoms leads in a reducing environment and at high temperatures to the creation of conduction electrons. This electronic compensation mechanism can be expressed using Kröger–Vink notation as



The electronic conductivity is then determined by the concentration of Ti^{3+} species, $[\text{Ti}^{3+}]$, and the mobility, μ_e , of the charge carriers [24,25].

$$\sigma_e = [\text{Ti}^{3+}] \times \mu_e \times e \quad (2)$$

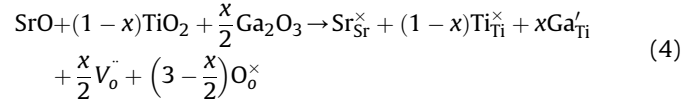
As a result, most doping strategies focus on increasing the concentration and mobility of the charge carriers, where the mobility of the electrons depends primarily on the crystal structure (e.g. type of cations, size, and symmetry of the unit cell) and microstructure (e.g. number of grain boundaries) [24]. In contrast, at high oxygen chemical potentials the extra charges generated by n-type dopants are compensated by the formation of Sr^{2+} cation vacancies. This type of charge compensation provides no conduction electrons and there is no improvement in electronic conductivity. For example, Kolodiaznyi and Petric [26] found that TiO_2 and niobium oxide second phases were formed when sintering $\text{Sr}_{1-x/2}\text{Ti}_{1-x}\text{Nb}_x\text{O}_3$ ($x = 0.17$) at low oxygen partial pressure and high temperature. This transformation can be expressed as



where $y < x \leq 0.2$.

In contrast to n-doping, the key function of p-type dopants is to enhance the ionic conductivity by improving the reducibility and number of oxygen vacancies in the material. Doping with p-type impurities generates electron holes in the host lattice, which can be compensated by introducing oxygen vacancies in the lattice. For

example, doping stoichiometric SrTiO_3 with Ga (p-type) impurities yields;



The amount of available oxygen vacancies plays an important role in the enhancement of the oxide ion diffusivity, D_O , in the lattice as evidenced by the following equation of the Random Walk model: [27]

$$D_O = \beta [V_0^\cdot] a^2 \nu_0 e^{-\Delta H_m / RT} \quad (5)$$

where $[V_0^\cdot]$ is the concentration of mobile vacancies, a is the cell parameter, ν_0 is a characteristic lattice frequency, ΔH_m is the enthalpy of vacancy migration, T is temperature, R is the ideal gas constant, and $\beta = (z/6)f e^{4S_m/R}$ is a function of the number of equivalent near-neighbor sites, z , the entropy of ion migration, ΔS_m , and a correction factor, f (≈ 1). It is noted that the mobile vacancy concentration is usually smaller than the stoichiometric concentration due to vacancy trapping or vacancy ordering [28,29]. This doping approach has led to the discovery of the compound $\text{La}_{1-x}\text{Sr}_x\text{Ga}_{1-y}\text{Mg}_y\text{O}_{3-\delta}$ with excellent oxide ion conductivity [30,31].

Lowering the oxygen chemical potential can result in more oxygen vacancies, leading to an excess electron density in the lattice. The reduction reaction takes place at the surface of the material and delivers electrons to the lattice [32].



The behavior of the electrons from oxygen vacancies is still ambiguous. While most studies report that Ti 3d states are involved in the formation of oxygen vacancies (which would increase the conductivity) [33,34], some studies suggest a partial or total localization of the electrons in the cavity [35,36] (which would not lead to an increase in conductivity). In our previous study we showed that the creation of oxygen vacancies in p-doped SrTiO_3 resulted in the formation of extra states in the band gap and a localization of charge [22,23]. This observation is in agreement with previous computational and experimental results that the electrons from oxygen vacancies are often localized and have little contribution to the electronic conductivity of the material [37–39].

As previously described, a mixed p- and n-doping approach has been suggested to improve mixed ionic/electronic conductivity in perovskite oxides. Our previous studies have shown that this doping strategy is efficient when doping with p-type dopants at the B-site and n-type dopants at either the A- or B-site of SrTiO_3 perovskites [22,23]. In this combined theoretical and experimental study, we illustrate that mixed p- and n-doping is indeed an efficient strategy independent of doping site in the SrTiO_3 perovskite structure. In particular, we performed constrained *ab initio* thermodynamic calculations to evaluate the thermodynamic stability of Na- and La-doped SrTiO_3 and Na- and Nb-doped SrTiO_3 phases at synthesized under oxidizing and under reducing anodic SOFC conditions. We analyzed the electronic structure of the resulting materials and compared the results to our previous study of Ga- and La-doped SrTiO_3 and Ga- and Nb-doped SrTiO_3 . Finally, we synthesized several compositions of Na- and La-doped SrTiO_3 and Na- and Nb-doped SrTiO_3 perovskites and measured their conductivities to confirm our computational predictions.

2. Methods

2.1. Computational approach

To investigate the bulk electronic properties of stoichiometric and doped SrTiO_3 , we initially optimized the lattice parameter of the SrTiO_3 unit cell and created a 100 atom supercell containing twenty unit cells ($5 \times 2 \times 2$). Doped structures were generated by substituting A- or B-site cations with various amount of n-type (La, Nb) and p-type (Na) dopants. Substitution of two Ti atoms with two dopants yields 10% B-site doped SrTiO_3 , etc. In order to better understand the charge compensation mechanism in the p- and n-doped systems, both A-site deficient and reduced structures were created by generating Sr vacancies and oxygen vacancies, respectively. In this study, we considered up to two Sr vacancies and three oxygen vacancies in each structure. The reoptimized lattice parameters of the 20% La-doped SrTiO_3 and 20% Nb-doped SrTiO_3 were employed for all La-doped and Nb-doped structures, respectively. We tried all meaningful configurations (over one hundred configurations were tested in this study) to identify the lowest energy structures.

Spin-polarized density functional theory was employed in this study using the projector-augmented wave approach [40] with Perdew–Burke–Ernzerhof (PBE) functional [41]. All calculations were performed with the VASP 5.2 code [40,42]. We use a kinetic energy cutoff of 400 eV for the plane wave basis and a $2 \times 5 \times 5$ Monkhorst–Pack k-point mesh for Brillouin zone integration [43]. For density of state (DOS) calculations we used a $4 \times 10 \times 10$ k-mesh. In all structure optimizations, all atoms are fully relaxed until the Hellman–Feynman forces are less than 0.02 eV \AA^{-1} .

Stoichiometric SrTiO_3 develops an ideal cubic perovskite structure at room temperature with $Pm3m$ space group. The cubic unit cell includes one molecular unit of SrTiO_3 . As shown in Fig. 1, the cubic SrTiO_3 structure contains 12-coordinated strontium ions occupying corner positions of the cube whereas the titanium ion, at the center of the cubic cell, is surrounded by six oxygen ions forming a TiO_6 octahedral unit. A sharing Ti–O–Ti bridge connects the octahedral units, forming a three-dimensional framework. Our calculated stoichiometric SrTiO_3 bulk unit cell has an optimized lattice constant of 3.948 \AA whereas the optimized 100 atom supercell yields the reduced-cell parameter of 3.920 \AA . The

calculated lattice parameters are in reasonable agreement to the experimental value of 3.90 \AA [44]. The optimized supercell of 20% La-doped SrTiO_3 and 20% Nb-doped SrTiO_3 exhibits only a very small change in lattice parameter to that of stoichiometric SrTiO_3 (3.921 and 3.949 \AA , respectively). As shown previously, the DOS of stoichiometric SrTiO_3 exhibits insulating behavior with a band gap of 1.80 eV [23]. While DFT within the GGA approximation is known to underestimate band gaps, several studies showed excellent agreement in predicted and experimentally observed electronic behavior of doped oxides computed by DFT within the GGA approximation [45–47]. Moreover, it has been shown that GGA–DFT can be used to predict formation energies and phase stabilities of several transition metal oxides [48].

It is important to note that we define the energy of atomic oxygen, E_O , to a half of the energy of an oxygen molecule, E_{O_2} , which is obtained from the H_2O splitting reaction using the experimental reaction energy and calculated DFT energies of H_2 and H_2O in the gas-phase [49,50].

$$E_{O_2} = 2 \left[(E_{\text{H}_2\text{O}}^{\text{DFT}} + E_{\text{H}_2\text{O}}^{\text{ZPE}}) - (E_{\text{H}_2}^{\text{DFT}} + E_{\text{H}_2}^{\text{ZPE}}) - E_{\text{hof}} \right] - E_{O_2}^{\text{ZPE}}, \quad (7)$$

where E^{ZPE} is the experimental zero point energy [51], E_{hof} is the experimental heat of formation of a gas-phase H_2O molecule [51], and E^{DFT} is the energy calculated with PBE functional.

2.2. Experimental approach

$\text{Sr}_{1-x}\text{Na}_x\text{Ti}_{0.8}\text{Nb}_{0.2}\text{O}_3$ ($x = 0, 0.05, 0.10, 0.20$) and $\text{Sr}_{0.8-x}\text{Na}_x\text{La}_{0.2}\text{TiO}_3$ ($x = 0, 0.10, 0.20$) powders were synthesized by standard solid state reactions. The starting materials include SrCO_3 (99%), TiO_2 (99.9%), Nb_2O_5 (99.9%, for Nb-doped samples), La_2O_3 (99%, for La-doped samples), and Na_2CO_3 (99%). The chemical constituents were carefully weighed according to the stoichiometry and mixed in a mortar. The mixed powder was calcined at $900 \text{ }^\circ\text{C}$ for 6 h in air. The powder was then ground, pressed into pellets and calcined at $1250 \text{ }^\circ\text{C}$ in air for 20 h. This step was repeated to improve the phase purity. The obtained powder was finally pressed into bar samples and sintered in 5% H_2/N_2 at $1400 \text{ }^\circ\text{C}$ for 10 h.

All samples were characterized by powder X-ray diffraction using a D/MAX-3C X-ray diffractometer with graphite-monochromatized $\text{Cu K}\alpha$ radiation in the 2θ range of $20\text{--}80^\circ$. Resistance of all bar samples with dimension of $35 \times 5 \times 1 \text{ mm}^3$ was recorded using a multimeter (Keithley model 2001 7-1/2 DDM) in a standard four probe configuration in H_2 with a flow rate of 80 ml min^{-1} . The samples were held at each temperature for 1 h before the data was collected.

3. Results and discussion

Previous theoretical studies performed by us [22,23] suggest that independent of n-doping site, mixed ionic/electronic conductivity of perovskites can be obtained when using a mixed p- and n-doping approach that uses a p-dopant concentration smaller than the n-dopant concentration. In this work, we aim to further prove that this doping strategy can be employed independent of p-doping site. Therefore, we performed DFT calculations of Na- and La-doped SrTiO_3 and Na- and Nb-doped SrTiO_3 . We used the same computational procedure as in our previous studies which permits us to systematically investigate the effects of doping site on the electronic conductivity and reducibility of the resulting structures at synthesized and anodic SOFC conditions. To a first approximation, we expect the electron mobility to remain constant when changing n-type dopants in doped SrTiO_3 since the difference in electron mobility between Nb- and La-doped SrTiO_3 is insignificant [52].

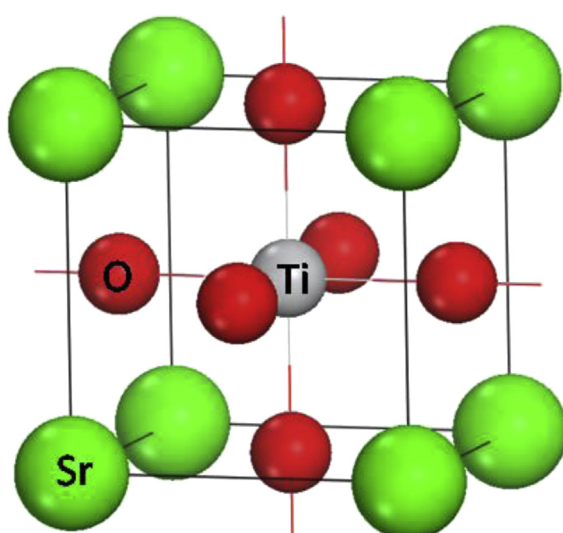


Fig. 1. Unit cell of SrTiO_3 perovskite oxide.

We first investigated the relative thermodynamic stability of all doped structures in each system using constrained *ab initio* thermodynamic simulations. The phase diagrams were constructed by calculating the free energy of different systems as a function of oxygen chemical potential, i.e., temperature and oxygen partial pressure. We neglect entropic contributions from the solids to the free energy differences and note that a reasonable estimate of the error in the calculated phase diagram is 0.2 eV considering that phonon contributions and configurational entropy likely only change on the order of 0.1–0.2 eV [53–55]. The reaction energies of the most dominant structures in the phase diagrams are summarized in Table 1. Next, the DOS related to the most dominant structures in the phase diagram were evaluated and analyzed with respect to relative electronic conductivity. Specifically, we computed the Fermi energy, μ , at 800 °C using equation (8)

$$N = \int_0^{\infty} d\epsilon D(\epsilon) f(\epsilon) \quad (8)$$

where N is the total number of electrons per supercell, $D(\epsilon)$ is the density of states at energy ϵ , and $f(\epsilon)$ is the Fermi–Dirac function, $f(\epsilon) = 1/(1 + \exp(\epsilon - \mu/k_B T))$, and then calculated the electron carrier, n_e , with

$$n_e = \int_{\mu}^{\infty} d\epsilon D(\epsilon) f(\epsilon) \quad (9)$$

and hole carriers, n_h , with

$$n_h = \int_0^{\mu} d\epsilon D(\epsilon) (1 - f(\epsilon)) \quad (10)$$

In the following, we assume that hole and electron carriers possess the same mobility such that the total number of charge carriers per supercell is the sum of electron and hole carriers. Figures of all structures found most stable at a specific oxygen chemical potential and the reaction energies of all structures considered can be found in the Supporting information.

3.1. Electronic structures and phase diagrams of 10% Na- and 20% La-doped SrTiO_3

To obtain a model of 10% Na- and 20% La-doped SrTiO_3 , we first replaced four Sr atoms with four La atoms in the $5 \times 2 \times 2$ supercell to create a structure of 20% La-doped SrTiO_3 . Next, we substituted another two Sr atoms with two Na atoms to generate a 10% Na- and 20% La-doped SrTiO_3 model. Furthermore, we removed one or two Sr atoms to create partial (5%) A-site deficient and full (10%) A-site deficient model structures, respectively. From the configuration of the most stable structures, we conclude that there is no long-range site preference for any Sr cation substitution with La or Na atoms since the energy differences of the most stable structures are insignificant (lower than 2 meV atom⁻¹). Only in the Sr-deficient structures do La atoms prefer to be close to Sr vacancies since the charge of the La dopants can be compensated by the presence of Sr vacancies. In an environment of low oxygen chemical potential (anodic SOFC conditions), the materials are reduced and oxygen vacancies start to form. We find that under these reducing conditions there is a tendency for oxygen vacancies to cluster close to nearby Na atoms. The extra electrons from the oxygen vacancies can be partially compensated by the holes created by the Na atoms in the structure.

Constrained *ab initio* thermodynamic calculations were performed to determine the approximate phase stability and reducibility of these structures at various temperatures and oxygen partial pressures. We employed two different types of calculations based on the main products that were generated upon the phase transition, i.e., a SrO rich second phase or $\text{TiO}_2/\text{Na}_2\text{O}/\text{La}_2\text{O}_3$ rich second phases. The details of these calculations can be found in our previous publication [22,23]. As shown in Fig. 2, the calculated phase diagrams of 10% Na- and 20% La-doped SrTiO_3 with SrO rich second phase and $\text{TiO}_2/\text{Na}_2\text{O}/\text{La}_2\text{O}_3$ rich second phases illustrate a phase transformation from 5% Sr-deficient structure to non Sr-deficient phase with increasing temperature and decreasing oxygen partial pressure. Further reduced structures are formed at high temperature and low oxygen partial pressure typical of SOFCs. The existence of a reduced structure indicates that Na-doping improves the reducibility of the material since in the absence of Na dopants only very few oxygen vacancies are observed [22].

Table 1
Summary of reaction energies used in constrained *ab initio* thermodynamic calculations.

Phase diagram	Reaction	ΔE (eV)
10% Na and 20% Nb-doped SrTiO_3 with SrO rich second phase	$\text{Sr}_{18}\text{Na}_2\text{Ti}_{16}\text{Nb}_4\text{O}_{60} + 1/2\text{O}_2 \rightarrow \text{Sr}_{17}\text{Na}_2\text{Ti}_{16}\text{Nb}_4\text{O}_{60} + \text{SrO}$ $\text{Sr}_{18}\text{Na}_2\text{Ti}_{16}\text{Nb}_4\text{O}_{60} \rightarrow \text{Sr}_{18}\text{Na}_2\text{Ti}_{16}\text{Nb}_4\text{O}_{59} + 1/2\text{O}_2$ $\text{Sr}_{18}\text{Na}_2\text{Ti}_{16}\text{Nb}_4\text{O}_{60} \rightarrow \text{Sr}_{18}\text{Na}_2\text{Ti}_{16}\text{Nb}_4\text{O}_{58} + \text{O}_2$ $\text{Sr}_{18}\text{Na}_2\text{Ti}_{16}\text{Nb}_4\text{O}_{60} \rightarrow \text{Sr}_{18}\text{Na}_2\text{Ti}_{16}\text{Nb}_4\text{O}_{57} + 3/2\text{O}_2$ $17\text{Sr}_{16}\text{Na}_2\text{Ti}_{16}\text{Nb}_4\text{O}_{60} \rightarrow 16\text{Sr}_{17}\text{Na}_2\text{Ti}_{16}\text{Nb}_4\text{O}_{60} + 16\text{TiO}_2 + 2\text{Nb}_2\text{O}_5 + \text{Na}_2\text{O} + 17/2\text{O}_2$ $9\text{Sr}_{16}\text{Na}_2\text{Ti}_{16}\text{Nb}_4\text{O}_{60} \rightarrow 8\text{Sr}_{18}\text{Na}_2\text{Ti}_{16}\text{Nb}_4\text{O}_{60} + 16\text{TiO}_2 + 2\text{Nb}_2\text{O}_5 + \text{Na}_2\text{O} + 17/2\text{O}_2$ $9\text{Sr}_{16}\text{Na}_2\text{Ti}_{16}\text{Nb}_4\text{O}_{60} \rightarrow 8\text{Sr}_{18}\text{Na}_2\text{Ti}_{16}\text{Nb}_4\text{O}_{59} + 16\text{TiO}_2 + 2\text{Nb}_2\text{O}_5 + \text{Na}_2\text{O} + 25/2\text{O}_2$ $9\text{Sr}_{16}\text{Na}_2\text{Ti}_{16}\text{Nb}_4\text{O}_{60} \rightarrow 8\text{Sr}_{18}\text{Na}_2\text{Ti}_{16}\text{Nb}_4\text{O}_{58} + 16\text{TiO}_2 + 2\text{Nb}_2\text{O}_5 + \text{Na}_2\text{O} + 33/2\text{O}_2$ $9\text{Sr}_{16}\text{Na}_2\text{Ti}_{16}\text{Nb}_4\text{O}_{60} \rightarrow 8\text{Sr}_{18}\text{Na}_2\text{Ti}_{16}\text{Nb}_4\text{O}_{57} + 16\text{TiO}_2 + 2\text{Nb}_2\text{O}_5 + \text{Na}_2\text{O} + 41/2\text{O}_2$ $\text{Sr}_{16}\text{Na}_4\text{Ti}_{16}\text{Nb}_4\text{O}_{60} \rightarrow \text{Sr}_{16}\text{Na}_4\text{Ti}_{16}\text{Nb}_4\text{O}_{59} + 1/2\text{O}_2$ $\text{Sr}_{16}\text{Na}_4\text{Ti}_{16}\text{Nb}_4\text{O}_{60} \rightarrow \text{Sr}_{16}\text{Na}_4\text{Ti}_{16}\text{Nb}_4\text{O}_{58} + \text{O}_2$ $\text{Sr}_{16}\text{Na}_4\text{Ti}_{16}\text{Nb}_4\text{O}_{60} \rightarrow \text{Sr}_{16}\text{Na}_4\text{Ti}_{16}\text{Nb}_4\text{O}_{57} + 3/2\text{O}_2$ $\text{Sr}_{14}\text{La}_4\text{Na}_2\text{Ti}_{20}\text{O}_{60} + 1/2\text{O}_2 \rightarrow \text{Sr}_{13}\text{La}_4\text{Na}_2\text{Ti}_{20}\text{O}_{60} + \text{SrO}$ $\text{Sr}_{14}\text{La}_4\text{Na}_2\text{Ti}_{20}\text{O}_{60} \rightarrow \text{Sr}_{14}\text{La}_4\text{Na}_2\text{Ti}_{20}\text{O}_{58} + \text{O}_2$ $\text{Sr}_{14}\text{La}_4\text{Na}_2\text{Ti}_{20}\text{O}_{60} \rightarrow \text{Sr}_{14}\text{La}_4\text{Na}_2\text{Ti}_{20}\text{O}_{57} + 3/2\text{O}_2$ $13\text{Sr}_{12}\text{La}_4\text{Na}_2\text{Ti}_{20}\text{O}_{60} \rightarrow 12\text{Sr}_{13}\text{La}_4\text{Na}_2\text{Ti}_{20}\text{O}_{60} + 20\text{TiO}_2 + 2\text{La}_2\text{O}_3 + \text{Na}_2\text{O} + 13/2\text{O}_2$ $7\text{Sr}_{12}\text{La}_4\text{Na}_2\text{Ti}_{20}\text{O}_{60} \rightarrow 6\text{Sr}_{14}\text{La}_4\text{Na}_2\text{Ti}_{20}\text{O}_{60} + 20\text{TiO}_2 + 2\text{La}_2\text{O}_3 + \text{Na}_2\text{O} + 13/2\text{O}_2$ $7\text{Sr}_{12}\text{La}_4\text{Na}_2\text{Ti}_{20}\text{O}_{60} \rightarrow 6\text{Sr}_{14}\text{La}_4\text{Na}_2\text{Ti}_{20}\text{O}_{58} + 20\text{TiO}_2 + 2\text{La}_2\text{O}_3 + \text{Na}_2\text{O} + 25/2\text{O}_2$ $7\text{Sr}_{12}\text{La}_4\text{Na}_2\text{Ti}_{20}\text{O}_{60} \rightarrow 6\text{Sr}_{14}\text{La}_4\text{Na}_2\text{Ti}_{20}\text{O}_{57} + 20\text{TiO}_2 + 2\text{La}_2\text{O}_3 + \text{Na}_2\text{O} + 31/2\text{O}_2$ $\text{Sr}_{12}\text{La}_4\text{Na}_4\text{Ti}_{20}\text{O}_{60} \rightarrow \text{Sr}_{12}\text{La}_4\text{Na}_4\text{Ti}_{20}\text{O}_{59} + 1/2\text{O}_2$ $\text{Sr}_{12}\text{La}_4\text{Na}_4\text{Ti}_{20}\text{O}_{60} \rightarrow \text{Sr}_{12}\text{La}_4\text{Na}_4\text{Ti}_{20}\text{O}_{58} + \text{O}_2$ $\text{Sr}_{12}\text{La}_4\text{Na}_4\text{Ti}_{20}\text{O}_{60} \rightarrow \text{Sr}_{12}\text{La}_4\text{Na}_4\text{Ti}_{20}\text{O}_{57} + 3/2\text{O}_2$	-2.08 4.84 10.00 15.36 -1.53 1.51 5.81 10.40 15.17 4.06 9.07 14.26 -1.46 10.03 15.39 0.57 4.68 13.46 18.15 4.46 9.43 14.54
10% Na and 20% Nb-doped SrTiO_3 with $\text{TiO}_2/\text{Na}_2\text{O}/\text{Nb}_2\text{O}_5$ rich second phases		
20% Na and 20% Nb-doped SrTiO_3		
10% Na and 20% La-doped SrTiO_3 with SrO rich second phase		
10% Na and 20% La-doped SrTiO_3 with $\text{TiO}_2/\text{Na}_2\text{O}/\text{La}_2\text{O}_3$ rich second phases		
20% Na and 20% La-doped SrTiO_3		

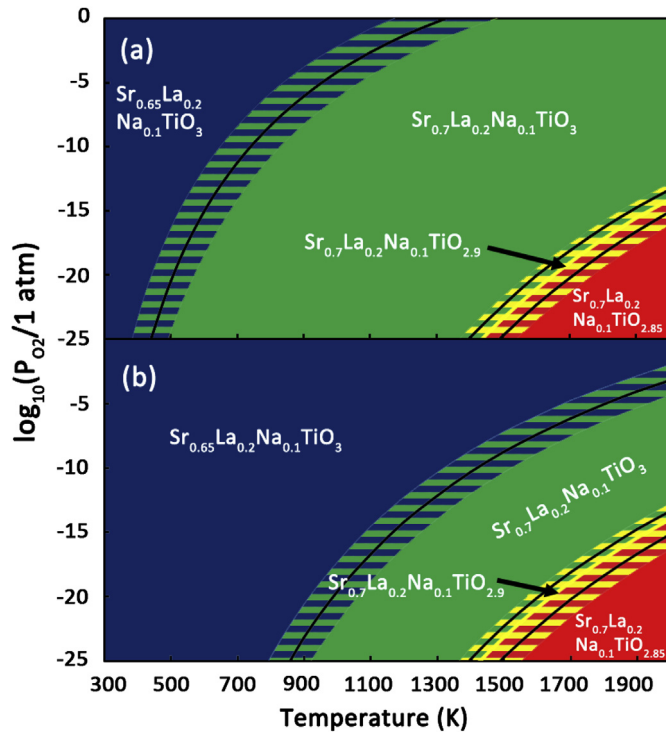


Fig. 2. Calculated phase diagram of 10% Na- and 20% La-doped SrTiO_3 with (a) SrO rich phase and (b) $\text{TiO}_2/\text{La}_2\text{O}_3/\text{Na}_2\text{O}$ rich phases. Differently shaded areas mark the stability region of various structures for a given temperature and partial pressure of oxygen. The hatched areas describe possible changes in the phase diagram if computed reaction energies shown in Table 1 are off by ± 0.2 eV (estimated error bar). Dark blue, green, yellow and red areas symbolize the stability of $\text{Sr}_{0.65}\text{La}_{0.2}\text{Na}_{0.1}\text{TiO}_3$, $\text{Sr}_{0.7}\text{La}_{0.2}\text{Na}_{0.1}\text{TiO}_3$, $\text{Sr}_{0.7}\text{La}_{0.2}\text{Na}_{0.1}\text{TiO}_{2.9}$, and $\text{Sr}_{0.7}\text{La}_{0.2}\text{Na}_{0.1}\text{TiO}_{2.85}$, respectively. (For interpretation of the references to color in this figure legend, the reader is referred to the web version of this article.)

The electronic conductivity of the most dominant structures in the phase diagram to a first approximation can be analyzed from their electronic structures. In particular, we performed DOS calculations and calculated the number of charge carriers per supercell to determine the degree of electronic conduction of the material. As illustrated in Fig. 3(a), the DOS of a 5% Sr-deficient phase exhibits insulating behavior since the charges from the four La dopants of the supercell are compensated by the presence of a Sr vacancy and electron holes generated from two Na dopants. A dramatic improvement in electronic conductivity is observed when the material is reduced. The DOS of the reduced structures exhibit metallic character as the Fermi energy shifts inside the conduction band with up to six electrons per supercell in the conduction band below the Fermi energy. Furthermore, partial density of states (PDOS) analyses were performed to evaluate the behavior of the electrons below the Fermi level in the conduction band and in the gap state. As reported in our previous studies, electrons in the gap state are mostly localized around the oxygen vacancies and thus do not contribute to the electronic conductivity of the material [22,23]. More interestingly, we observe that the electrons closest to the Fermi level in the conduction band are delocalized and do contribute to the electronic conductivity. Fig. 4 depicts the PDOS and their respective charge densities obtained from band decomposition charge density calculations of $\text{Sr}_{0.7}\text{La}_{0.2}\text{Na}_{0.1}\text{TiO}_{2.9}$. It can be seen that the electrons act differently in the two different energy regions. In the lower energy range (-0.3 to -0.2 eV), the electrons are mostly localized around oxygen vacancies and surrounded atoms whereas the electrons in the higher energy range (-0.2 to 0 eV)

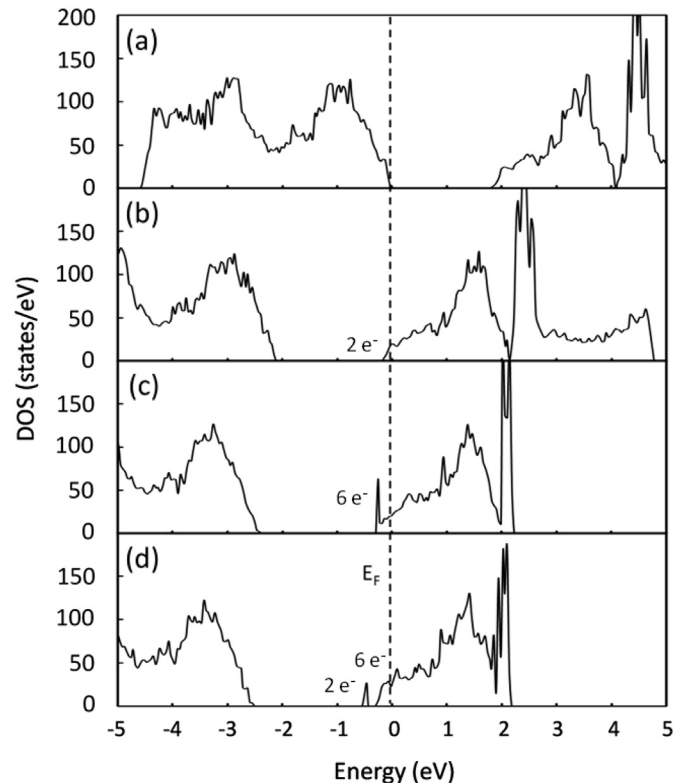


Fig. 3. Density of states of (a) $\text{Sr}_{0.65}\text{La}_{0.2}\text{Na}_{0.1}\text{TiO}_3$, (b) $\text{Sr}_{0.7}\text{La}_{0.2}\text{Na}_{0.1}\text{TiO}_3$, (c) $\text{Sr}_{0.7}\text{La}_{0.2}\text{Na}_{0.1}\text{TiO}_{2.9}$, and (d) $\text{Sr}_{0.7}\text{La}_{0.2}\text{Na}_{0.1}\text{TiO}_{2.85}$. The Fermi level is set to zero on the energy scale. Numbers of electrons shown in the figure indicate the integrated number of electrons per supercell for the specified DOS area at zero Kelvin, i.e., states in the band gap and states below the Fermi level.

0 eV) are delocalized throughout the Ti atoms in the lattice. The localized electrons in the low energy region do not contribute significantly to the electronic conductivity of the material (both because of their distance to the Fermi level and their likely low mobility); however, the electrons closest to the Fermi level contribute significantly to the conductivity and the calculated number of charge carriers per supercell at 800 °C for the $\text{Sr}_{0.7}\text{La}_{0.2}\text{Na}_{0.1}\text{TiO}_{2.9}$ and $\text{Sr}_{0.7}\text{La}_{0.2}\text{Na}_{0.1}\text{TiO}_{2.85}$ structures are 2.36

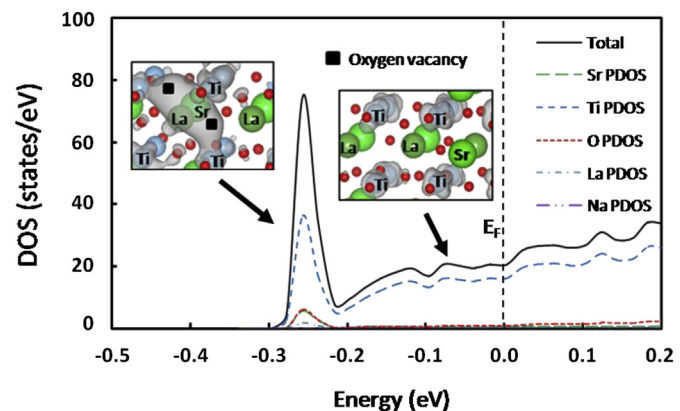


Fig. 4. Partial density of states of $\text{Sr}_{0.7}\text{La}_{0.2}\text{Na}_{0.1}\text{TiO}_{2.9}$ below the Fermi level in the conduction band. The left inset illustrates the charge density of the localized states which are located at the oxygen vacancy (energy ranges between -0.3 and -0.2 eV). The right inset describes the charge density of delocalized states from mixed-valent $\text{Ti}^{3+}/\text{Ti}^{4+}$ found in the energy range between -0.2 and 0 eV.

and 2.99, respectively. The calculated number of charge carriers for all p- and n-doped SrTiO_3 structures considered in this work are summarized in Table 2.

3.2. Electronic structures and phase diagrams of 20% Na- and 20% La-doped SrTiO_3

Substitution of four Sr atoms with four Na atoms in 20% La-doped structures leads to 20% Na- and 20% La-doped SrTiO_3 . The presence of Sr and oxygen vacancies in the structure was investigated in a similar manner as described above. The most dominant structures display a random configuration of La and Na atoms since the energy difference of the lowest energy structures is insignificant (lower than 2 meV atom⁻¹). On the other hand, the most stable reduced structures have oxygen vacancies surrounded by the four Na atoms of the supercell (see *Supporting information* for structures). Such preferred configurations confirm that the charge compensation mechanism plays an essential role in the arrangement of impurities in the structure.

The calculated phase diagram of this system obtained from constrained *ab initio* thermodynamic simulations is illustrated in Fig. 5. Since the Sr-deficient structures are not stable in this system, there are no SrO or $\text{TiO}_2/\text{Na}_2\text{O}/\text{La}_2\text{O}_3$ rich second phases. Interestingly, increasing the Na content from 10% to 20% in 20% La-doped SrTiO_3 does not lead to a significant improvement of the reducibility of the material. Moreover, the number of charge carriers obtained from DOS and PDOS analyses reveal that increasing the amount of Na dopants leads to a reduction in the electronic conductivity. As shown in Fig. 6, the states below the Fermi level in the conduction band of the reduced structures contain up to four electrons and the number of charge carriers at 800 °C are 1.57, 2.32,

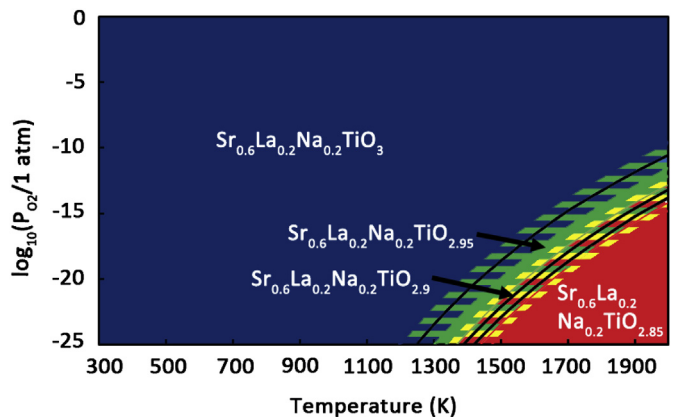


Fig. 5. Calculated phase diagram of 20% Na- and 20% La-doped SrTiO_3 . Differently shaded areas mark the stability region of various structures for a given temperature and partial pressure of oxygen. The hatched areas describe possible changes in the phase diagram if computed reaction energies shown in Table 1 are off by ± 0.2 eV (estimated error bar). Dark blue, green, yellow, and red areas symbolize the stability of $\text{Sr}_{0.6}\text{La}_{0.2}\text{Na}_{0.2}\text{TiO}_3$, $\text{Sr}_{0.6}\text{La}_{0.2}\text{Na}_{0.2}\text{TiO}_{2.95}$, $\text{Sr}_{0.6}\text{La}_{0.2}\text{Na}_{0.2}\text{TiO}_{2.9}$, and $\text{Sr}_{0.6}\text{La}_{0.2}\text{Na}_{0.2}\text{TiO}_{2.85}$, respectively. (For interpretation of the references to color in this figure legend, the reader is referred to the web version of this article.)

and 2.56 per supercell for $\text{Sr}_{0.6}\text{La}_{0.2}\text{Na}_{0.2}\text{TiO}_{2.95}$, $\text{Sr}_{0.6}\text{La}_{0.2}\text{Na}_{0.2}\text{TiO}_{2.90}$, and $\text{Sr}_{0.6}\text{La}_{0.2}\text{Na}_{0.2}\text{TiO}_{2.85}$, respectively (see also Table 2). Thus, while doping with 20% Na improves the ionic conductivity (though not significantly more than 10% Na-doping), the electronic conductivity is likely diminished under realistic fuel cell operating conditions.

Table 2
Summary of total and electron charge carriers per supercell in doped SrTiO_3 at 800 °C.

Structure	Number of total carriers (number of electron carriers)
20% Nb-doped SrTiO_3	1.82 (1.18)
10% Ga- and 20% Nb-doped SrTiO_3	
$\text{SrTi}_{0.7}\text{Nb}_{0.2}\text{Ga}_{0.1}\text{O}_{2.95}$	1.84 (1.19)
$\text{SrTi}_{0.7}\text{Nb}_{0.2}\text{Ga}_{0.1}\text{O}_{2.90}$	1.71 (1.07)
$\text{SrTi}_{0.7}\text{Nb}_{0.2}\text{Ga}_{0.1}\text{O}_{2.85}$	1.67 (1.04)
20% Ga- and 20% Nb-doped SrTiO_3	
$\text{SrTi}_{0.6}\text{Nb}_{0.2}\text{Ga}_{0.2}\text{O}_{2.95}$	1.65 (1.46)
$\text{SrTi}_{0.6}\text{Nb}_{0.2}\text{Ga}_{0.2}\text{O}_{2.90}$	1.54 (1.32)
$\text{SrTi}_{0.6}\text{Nb}_{0.2}\text{Ga}_{0.2}\text{O}_{2.85}$	1.47 (1.24)
10% Na- and 20% Nb-doped SrTiO_3	
$\text{Sr}_{0.9}\text{Na}_{0.1}\text{Ti}_{0.8}\text{Nb}_{0.2}\text{O}_{2.95}$	1.87 (1.24)
$\text{Sr}_{0.9}\text{Na}_{0.1}\text{Ti}_{0.8}\text{Nb}_{0.2}\text{O}_{2.90}$	2.10 (1.34)
$\text{Sr}_{0.9}\text{Na}_{0.1}\text{Ti}_{0.8}\text{Nb}_{0.2}\text{O}_{2.85}$	2.05 (1.28)
20% Na- and 20% Nb-doped SrTiO_3	
$\text{Sr}_{0.8}\text{Na}_{0.2}\text{Ti}_{0.8}\text{Nb}_{0.2}\text{O}_{2.95}$	1.47 (1.18)
$\text{Sr}_{0.8}\text{Na}_{0.2}\text{Ti}_{0.8}\text{Nb}_{0.2}\text{O}_{2.90}$	2.06 (1.45)
$\text{Sr}_{0.8}\text{Na}_{0.2}\text{Ti}_{0.8}\text{Nb}_{0.2}\text{O}_{2.85}$	2.00 (1.31)
20% La-doped SrTiO_3	1.96 (1.29)
10% Ga- and 20% La-doped SrTiO_3	
$\text{Sr}_{0.8}\text{La}_{0.2}\text{Ti}_{0.9}\text{Ga}_{0.1}\text{O}_{2.90}$	2.01 (1.44)
$\text{Sr}_{0.8}\text{La}_{0.2}\text{Ti}_{0.9}\text{Ga}_{0.1}\text{O}_{2.85}$	1.96 (1.34)
20% Ga- and 20% La-doped SrTiO_3	
$\text{Sr}_{0.8}\text{La}_{0.2}\text{Ti}_{0.8}\text{Ga}_{0.2}\text{O}_{2.90}$	1.30 (1.02)
$\text{Sr}_{0.8}\text{La}_{0.2}\text{Ti}_{0.8}\text{Ga}_{0.2}\text{O}_{2.85}$	1.52 (1.20)
10% Na- and 20% La-doped SrTiO_3	
$\text{Sr}_{0.7}\text{La}_{0.2}\text{Na}_{0.1}\text{TiO}_{2.90}$	2.36 (1.55)
$\text{Sr}_{0.7}\text{La}_{0.2}\text{Na}_{0.1}\text{TiO}_{2.85}$	2.99 (1.98)
20% Na- and 20% La-doped SrTiO_3	
$\text{Sr}_{0.6}\text{La}_{0.2}\text{Na}_{0.2}\text{TiO}_{2.95}$	1.57 (1.30)
$\text{Sr}_{0.6}\text{La}_{0.2}\text{Na}_{0.2}\text{TiO}_{2.90}$	2.32 (1.47)
$\text{Sr}_{0.6}\text{La}_{0.2}\text{Na}_{0.2}\text{TiO}_{2.85}$	2.56 (1.89)

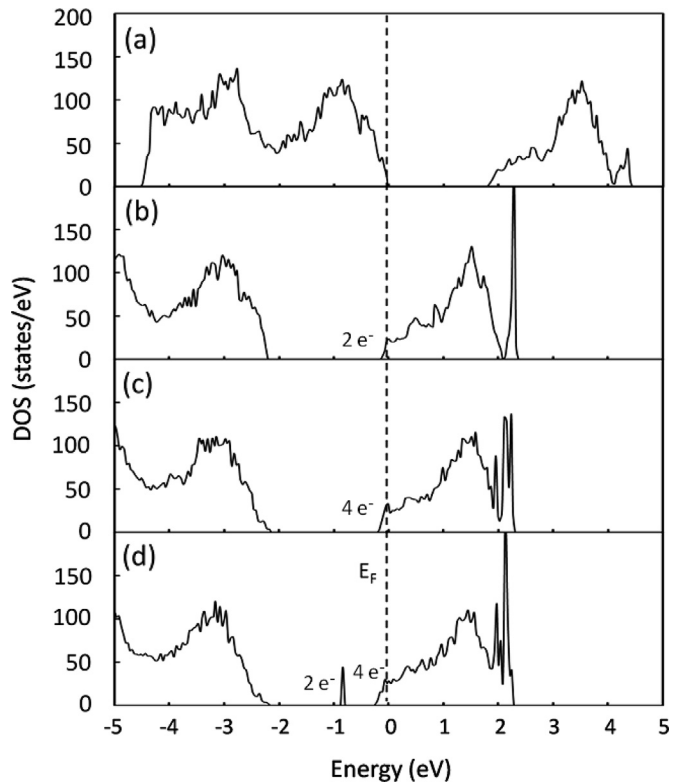


Fig. 6. Density of states of (a) $\text{Sr}_{0.6}\text{La}_{0.2}\text{Na}_{0.2}\text{TiO}_3$, (b) $\text{Sr}_{0.6}\text{La}_{0.2}\text{Na}_{0.2}\text{TiO}_{2.95}$, (c) $\text{Sr}_{0.6}\text{La}_{0.2}\text{Na}_{0.2}\text{TiO}_{2.9}$, and (d) $\text{Sr}_{0.6}\text{La}_{0.2}\text{Na}_{0.2}\text{TiO}_{2.85}$. The Fermi level is set to zero on the energy scale. Numbers of electrons shown in the figure indicate the integrated number of electrons per supercell for the specified DOS area at zero Kelvin, i.e., states in the band gap and states below the Fermi level.

3.3. Electronic structures and phase diagrams of 10% Na- and 20% Nb-doped SrTiO_3

In this set of calculations, we first created a 20% Nb-doped SrTiO_3 structure by replacing four Ti atoms with four Nb atoms in the $5 \times 2 \times 2$ supercell. Next, we substituted two Sr atoms with two Na atoms in the 20% Nb-doped SrTiO_3 structure to obtain a model of 10% Na- and 20% Nb-doped SrTiO_3 . To study the cation vacancy compensation mechanism, we created up to two Sr vacancies in the lattice to obtain Sr-deficient structures as described previously. The most stable structures reveal that Nb and Na impurities prefer to be in close proximity since the extra electron from the Nb dopants can be compensated by the electron holes generated from the Na dopants. This preferred configuration is also observed in the presence of Sr vacancies. Up to three oxygen vacancies were generated in the structure to study the effect of a reducing environment typical of anodic SOFC conditions. The most stable first vacancy is created by removing an oxygen atom from a Ti–O–Ti bridge close to Na dopants whereas the second oxygen vacancy is positioned next to the same Ti atom. Upon removal of the third oxygen, a row of oxygen vacancies is formed along the TiO_6 octahedra framework.

Fig. 7 displays the calculated phase diagrams of 10% Na- and 20% Nb-doped SrTiO_3 under synthesized and anodic SOFC conditions leading to the formation of a SrO rich second phase (Fig. 7(a)) and $\text{TiO}_2/\text{Nb}_2\text{O}_5/\text{NaO}$ rich second phases (Fig. 7(b)). It can be seen from the phase diagrams that the phase transitions of this system are very similar to those of the 10% Na- and 20% La-doped system, i.e., the presence of 5% Sr-deficient, non Sr-deficient, and reduced

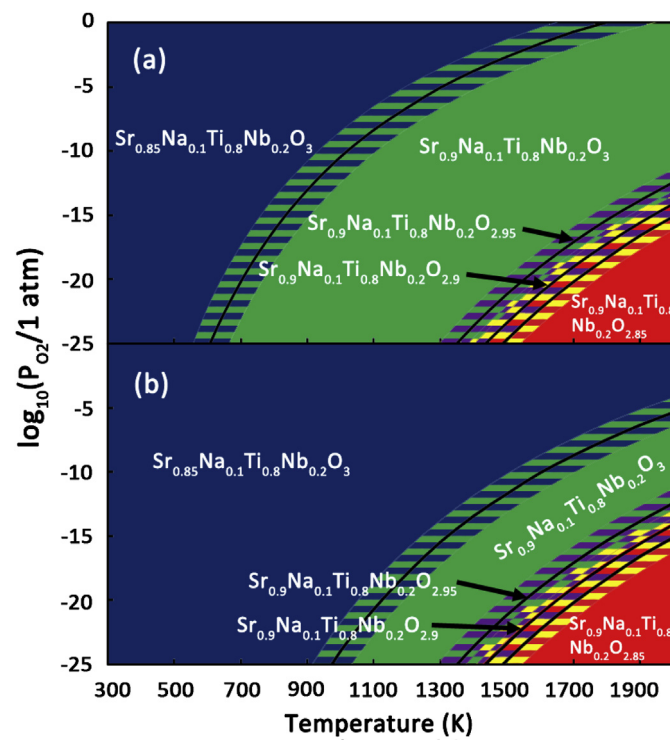


Fig. 7. Calculated phase diagram of 10% Na- and 20% Nb-doped SrTiO_3 with (a) SrO rich phase and (b) $\text{TiO}_2/\text{Nb}_2\text{O}_5/\text{NaO}$ rich phases. Differently shaded areas mark the stability region of various structures for a given temperature and partial pressure of oxygen. The hatched areas describe possible changes in the phase diagram if computed reaction energies shown in Table 1 are off by ± 0.2 eV (estimated error bar). Dark blue, green, purple, yellow and red areas symbolize the stability of $\text{Sr}_{0.85}\text{Na}_{0.1}\text{Ti}_{0.8}\text{Nb}_{0.2}\text{O}_3$, $\text{Sr}_{0.9}\text{Na}_{0.1}\text{Ti}_{0.8}\text{Nb}_{0.2}\text{O}_3$, $\text{Sr}_{0.9}\text{Na}_{0.1}\text{Ti}_{0.8}\text{Nb}_{0.2}\text{O}_{2.95}$, $\text{Sr}_{0.9}\text{Na}_{0.1}\text{Ti}_{0.8}\text{Nb}_{0.2}\text{O}_{2.9}$, and $\text{Sr}_{0.9}\text{Na}_{0.1}\text{Ti}_{0.8}\text{Nb}_{0.2}\text{O}_{2.85}$, respectively. (For interpretation of the references to color in this figure legend, the reader is referred to the web version of this article.)

phases of both systems occur at approximately the same temperature and oxygen partial pressure. Again, the presence of the reduced phases in this system confirms that Na facilitates oxide ion conduction as the reducibility of the material has been improved. The electronic structures of the reduced phases exhibit up to six electrons per supercell below the Fermi energy in the conduction band. As shown in Fig. 8, the DOS of 10% Na- and 20% Nb-doped SrTiO_3 reveal that the electronic conductivity is remarkably improved when the material is reduced under anodic SOFC conditions. The electronic conductivity of these reduced structures are comparable (though slightly smaller) to those of 10% Na- and 20% La-doped SrTiO_3 since the number of charge carriers at 800 °C are up to 2.1 per supercell (Table 2).

3.4. Electronic structures and phase diagrams of 20% Na- and 20% Nb-doped SrTiO_3

Substitution of four Sr atoms with four Na atoms in the 20% Nb-doped SrTiO_3 structure yields a model of 20% Na- and 20% Nb-doped SrTiO_3 . Sr-deficient and reduced structures were created to investigate the charge compensation mechanism in the presence of Sr vacancies and oxygen vacancies. The most stable structures in this set of calculations have Na atoms close to Nb atoms. Again, it is preferable to create the first and second oxygen vacancies at the Ti–O–Ti bridge where two oxygen vacancies share the same Ti atom

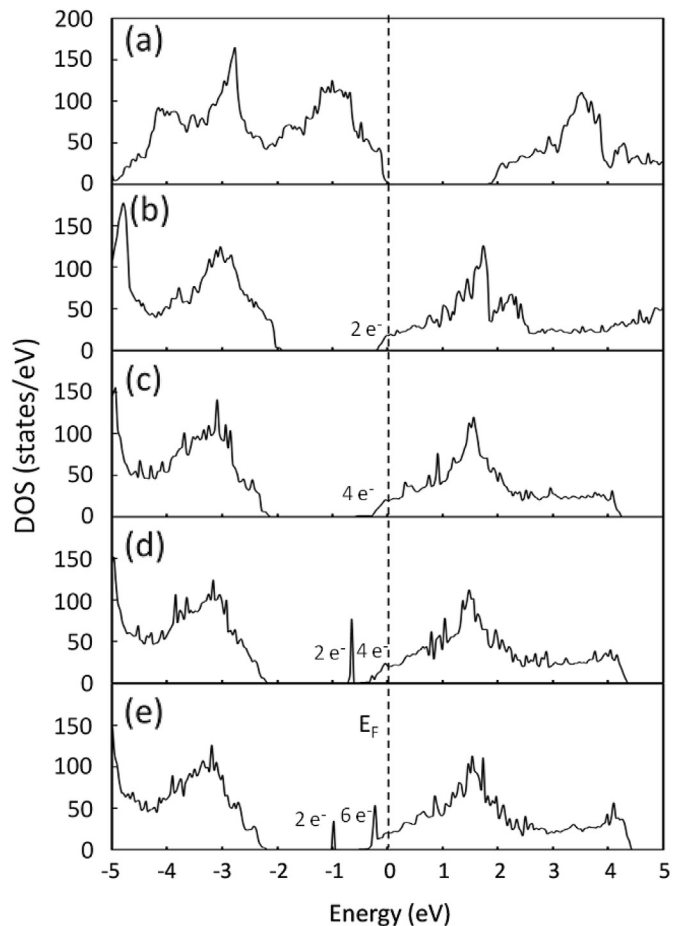


Fig. 8. Density of states of (a) $\text{Sr}_{0.85}\text{Na}_{0.1}\text{Ti}_{0.8}\text{Nb}_{0.2}\text{O}_3$, (b) $\text{Sr}_{0.9}\text{Na}_{0.1}\text{Ti}_{0.8}\text{Nb}_{0.2}\text{O}_3$, (c) $\text{Sr}_{0.9}\text{Na}_{0.1}\text{Ti}_{0.8}\text{Nb}_{0.2}\text{O}_{2.95}$, (d) $\text{Sr}_{0.9}\text{Na}_{0.1}\text{Ti}_{0.8}\text{Nb}_{0.2}\text{O}_{2.90}$ and (e) $\text{Sr}_{0.9}\text{Na}_{0.1}\text{Ti}_{0.8}\text{Nb}_{0.2}\text{O}_{2.85}$. The Fermi level is set to zero on the energy scale. Numbers of electrons shown in the figure indicate the integrated number of electrons per supercell for the specified DOS area at zero Kelvin, i.e., states below the Fermi level.

forming a TiO_4 unit, whereas the third oxygen vacancy is positioned at another $\text{Ti}-\text{O}-\text{Ti}$ bridge nearby generating a TiO_5 unit. These three oxygen vacancies are close to the Na atoms, which confirms that electrons from oxygen vacancies are partially compensated by holes generated from the Na dopants.

Fig. 9 illustrates the phase diagram for 20% Na - and 20% Nb -doped SrTiO_3 as a function of temperature and oxygen partial pressure. Unlike Na - and La -doped SrTiO_3 , increasing the Na concentration in this system does improve the reducibility of the material. As seen in the phase diagram, at an oxygen partial pressure of 10^{-20} atm the reduced phases of 20% Na - and 20% Nb -doped SrTiO_3 start to develop 200 K below when those are formed for the 10% Na -doped system. However, adding too much Na results in a decreasing electronic conductivity. The DOS of the reduced structures of this system (Fig. 10) exhibit states below the Fermi level in the conduction band that contain up to four electrons per supercell. Nevertheless, charge carrier calculations show that the degree of electronic conductivity of this system is generally lower than that of the 10% Na -doped system (Table 2). The concentration of conduction electrons in the lattice is reduced by the large amounts of electron holes from the Na dopants.

3.5. Experimental verification of computational predictions

To study the effect of p-doping on the mixed ionic/electronic conductivity and to confirm our computational predictions, Na - and Nb -doped SrTiO_3 and Na - and La -doped SrTiO_3 samples were prepared at 1250 °C in air and reduced in 5% H_2/N_2 at 1400 °C. Powder X-ray diffraction (PXRD) patterns of $\text{Sr}_{1-x}\text{Na}_x\text{Ti}_{0.8}\text{Nb}_{0.2}\text{O}_3$ (where $x = 0, 0.05, 0.10, 0.20$) and $\text{Sr}_{0.8-x}\text{Na}_x\text{La}_{0.2}\text{Ti}_{0.8}\text{Nb}_{0.2}\text{O}_3$ (where $x = 0, 0.10, 0.20$) calcined under oxidizing conditions are depicted in Fig. 11a) and b), respectively. The presence of impurity peaks for all samples other than $\text{Sr}_{0.8}\text{Na}_{0.2}\text{Ti}_{0.8}\text{Nb}_{0.2}\text{O}_3$ indicates that due to a lack of charge compensation, these compositions cannot form under oxidizing conditions where Ti and Nb are in their highest oxidation states. Since the extra charges from the n-type dopants (Nb or La) cannot be electronically compensated under oxidizing conditions, these extra electrons are instead neutralized by creating Sr vacancies in the lattice (cation vacancy compensation), which creates Sr rich impurity phases. The main impurity

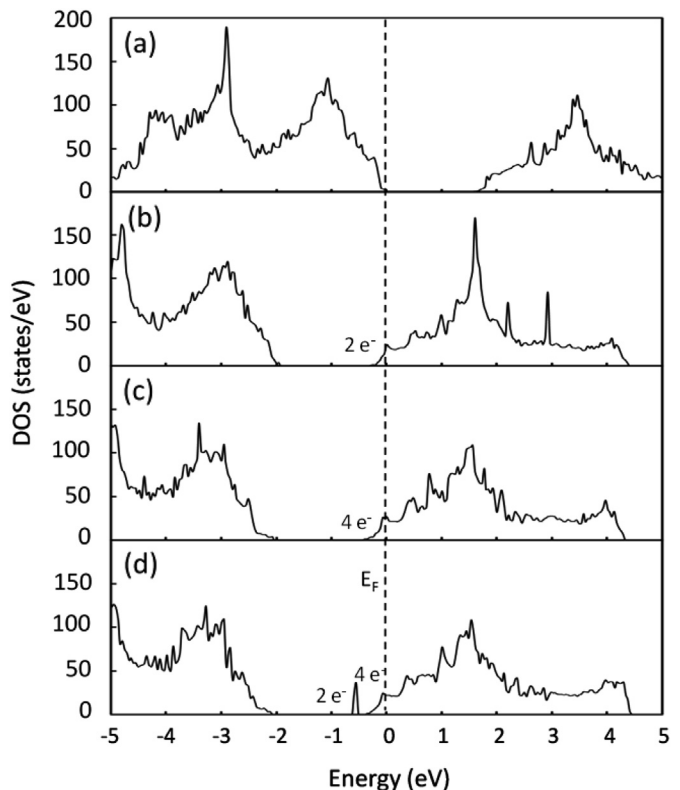


Fig. 10. Density of states of (a) $\text{Sr}_{0.8}\text{Na}_{0.2}\text{Ti}_{0.8}\text{Nb}_{0.2}\text{O}_3$, (b) $\text{Sr}_{0.8}\text{Na}_{0.2}\text{Ti}_{0.8}\text{Nb}_{0.2}\text{O}_{2.95}$, (c) $\text{Sr}_{0.8}\text{Na}_{0.2}\text{Ti}_{0.8}\text{Nb}_{0.2}\text{O}_{2.9}$, and (d) $\text{Sr}_{0.8}\text{Na}_{0.2}\text{Ti}_{0.8}\text{Nb}_{0.2}\text{O}_{2.85}$. The Fermi level is set to zero on the energy scale. Numbers of electrons shown in the figure indicate the integrated number of electrons per supercell for the specified DOS area at zero Kelvin, i.e., states below the Fermi level.

phase in Fig. 11a) can be attributed to $\text{Sr}_5\text{Nb}_4\text{O}_{15}$ (JCPDS file no. 48-0421). In La -doped SrTiO_3 , it has been reported that under oxidizing conditions the extra oxygen can be accommodated by $\text{La}_2\text{Ti}_2\text{O}_7$ -type layers. No cation vacancy is required in this mechanism. At low doping concentrations, for example 20% in our work, the impurity peaks in XRD are less evident [56]. Increasing the concentration of Na (p-type) dopants leads eventually to charge compensation and stable phases since now the extra electrons from the n-type dopants are compensated by electron holes generated from the Na dopants. In agreement with this observation, it has been reported that p-type doping significantly promotes oxygen loss from the structure and enhances oxygen diffusion in the materials [21,24]. These experimental findings are in an excellent agreement with our theoretical predictions, suggesting that p-doping (Na or Ga) improves the reducibility of the materials [24].

To perform conductivity measurements, all samples were pressed into bar samples and sintered in reducing atmosphere at 1400 °C. The conductivities of the doped SrTiO_3 samples were then measured under reducing conditions. We find that p-type doping allows not only for the formation of a stable, reduced phase, but also enhances the electrical conductivity of the samples. Fig. 12 illustrates the electrical conductivity of Na - and Nb -doped SrTiO_3 as a function of Na concentration at different temperatures. In a reducing atmosphere at high temperatures, Na - and Nb -doped SrTiO_3 samples exhibit metallic behavior as their conductivity decreases when the temperature increases. The conductivity shows a maximum at 5% Na concentration and decreases abruptly when increasing the doping concentration to 10% and 20%. At high Na concentration the conduction electrons from the Nb dopants seem to be mostly compensated by the hole doping effect of Na leading to

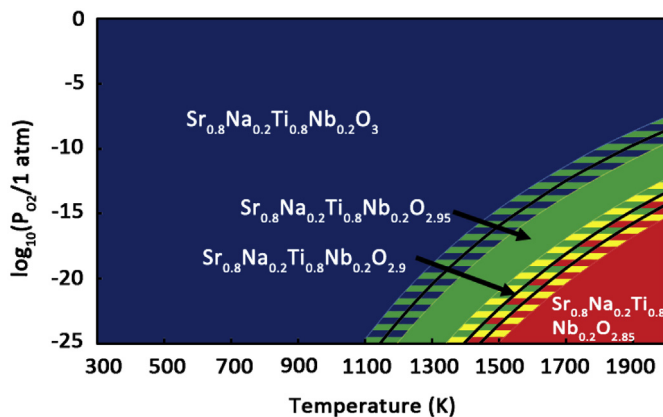


Fig. 9. Calculated phase diagram of 20% Na - and 20% Nb -doped SrTiO_3 . Differently shaded areas mark the stability region of various structures for a given temperature and partial pressure of oxygen. The hatched areas describe possible changes in the phase diagram if computed reaction energies shown in Table 1 are off by ± 0.2 eV (estimated error bar). Dark blue, green, yellow, and red areas symbolize the stability of $\text{Sr}_{0.8}\text{Na}_{0.2}\text{Ti}_{0.8}\text{Nb}_{0.2}\text{O}_3$, $\text{Sr}_{0.8}\text{Na}_{0.2}\text{Ti}_{0.8}\text{Nb}_{0.2}\text{O}_{2.95}$, $\text{Sr}_{0.8}\text{Na}_{0.2}\text{Ti}_{0.8}\text{Nb}_{0.2}\text{O}_{2.9}$, and $\text{Sr}_{0.8}\text{Na}_{0.2}\text{Ti}_{0.8}\text{Nb}_{0.2}\text{O}_{2.85}$, respectively. (For interpretation of the references to color in this figure legend, the reader is referred to the web version of this article.)

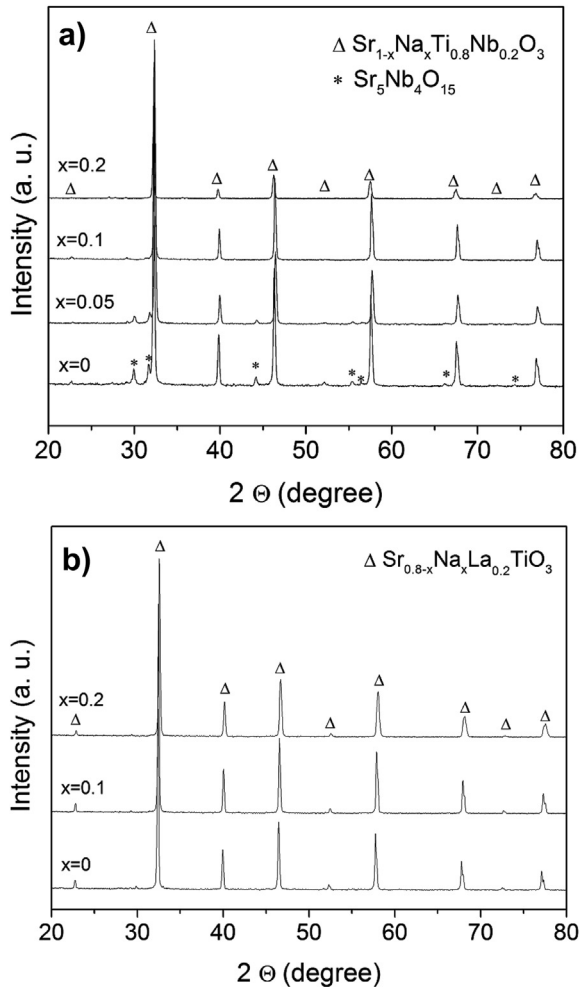


Fig. 11. XRD pattern of a) $\text{Sr}_{1-x}\text{Nax}\text{Ti}_{0.8}\text{Nb}_{0.2}\text{O}_3$ powder and b) $\text{Sr}_{0.8-x}\text{Nax}\text{La}_{0.2}\text{TiO}_3$ powder after solid state reactions at 1250 °C in air.

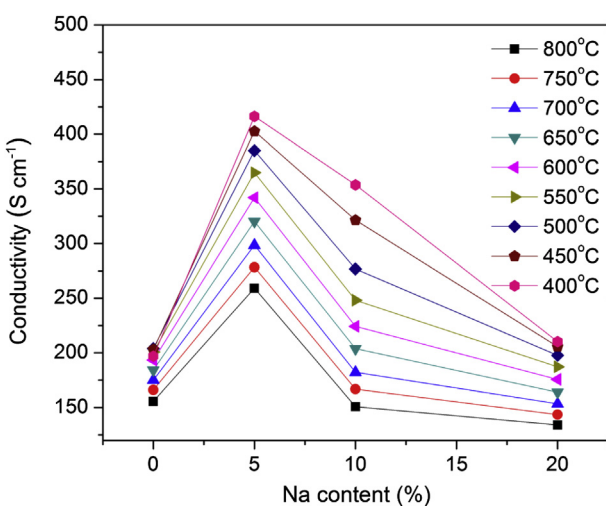


Fig. 12. Electrical conductivity of $\text{Sr}_{1-x}\text{Nax}\text{Ti}_{0.8}\text{Nb}_{0.2}\text{O}_3$ samples sintered in 5% H_2/N_2 ($\text{pO}_2 \sim 10^{-22}$ bar at 800 °C) at 1400 °C as a function of temperature and Na content. The conductivity was measured in H_2 with a flow rate of 80 ml min⁻¹ ($\text{pO}_2 \sim 10^{-26}$ bar at 800 °C).

a reduction in the electronic conductivity, in excellent qualitative agreement with our calculations that doping with only small amounts of Na significantly improves the electronic conductivity since a small concentration of electron holes can be compensated by the presence of oxygen vacancies in the lattice.

It is interesting to note that stoichiometric and A-site deficient 20% La-doped SrTiO_3 samples do not exhibit metallic behavior as expected. Instead, these samples show semiconducting behavior with low conductivity as shown in Fig. 13. We believe this behavior can be explained by the poor phase stability of the La-doped SrTiO_3 samples [56] which leads to the low incorporation of La in the samples even when these samples were exposed to a reducing atmosphere at high temperatures. Since the concentration of conduction electrons depends strongly on the level of La dopants in the lattice, the samples with low La concentration exhibit a small concentration of conduction electrons. According to Mott's theory [56,57], a transition from semiconducting to metallic behavior may occur if the concentration of conduction electrons exceeds a critical value. In this particular case, the number of conduction electrons that 20% La-doped SrTiO_3 samples possess may not surpass this value and we observe semiconducting behavior and low conductivity for these samples. This semiconducting behavior has also been reported in Y-doped SrTiO_3 systems [56].

We want to emphasize that Na-doping improves the formation, reducibility, and mixed ionic/electronic conductivity of the materials. Fig. 13 shows that doping 20% La-doped SrTiO_3 with small amounts of Na remarkably increases the conductivity of the materials. The improvement in conductivity originates from the improved reducibility and increased number of charge carriers (as discussed above) of the Na-doped materials. Note that small amounts of Na do not diminish the electronic conductivity of the materials since the hole doping effect from Na dopants is compensated by the presence of oxygen vacancies in the material. Furthermore, the number of oxygen vacancies produced in the lattice could support oxide ion conductivity of the material. As a result, the materials become mixed ionic/electronic conductors. However, as predicted above adding too much Na diminishes the electronic conductivity because the concentration of charge carriers in the lattice is reduced by the effects of electron–hole compensation due to the large amount of Na dopants in the materials. As can be seen from Fig. 13, the conductivity drops by a half when increasing the concentration of Na from 10% to 20%. Moreover, using Na as a p-type dopant in p- and n-doped SrTiO_3 results

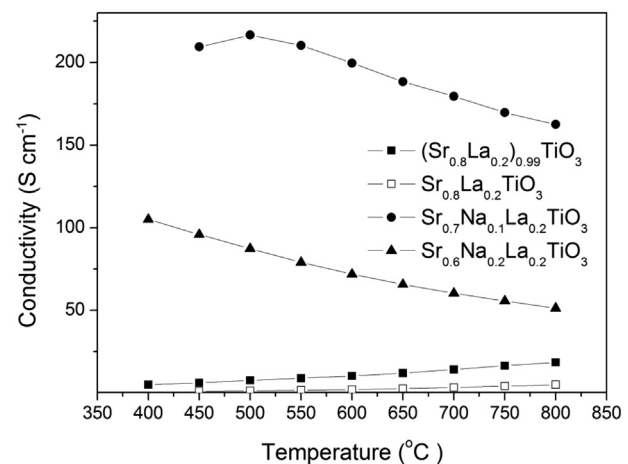


Fig. 13. Temperature dependence of the conductivity of $\text{Sr}_{0.8-x}\text{Nax}\text{La}_{0.2}\text{TiO}_3$ samples sintered in 5% H_2/N_2 at 1400 °C. The conductivity was measured in H_2 with a flow rate of 80 ml min⁻¹.

in a higher conductivity than using Ga [22,23]. As shown in Table 2, the calculated number of charge carriers in Na- and n- (La or Nb) doped SrTiO_3 perovskites are generally higher than those of Ga- and n- (La or Nb) doped SrTiO_3 perovskites. The computational predictions are in excellent agreement with the experimental results [21,24]. The only inconsistency between experimental observations and calculated results is that computations predict that the Na- and La-doped system exhibits a higher conductivity than the Na- and Nb-doped systems, while our experimental measurements clearly indicate that the Na- and Nb-doped system displays a higher total conductivity. We attribute this inconsistency to a lower mobility of the charge carriers and reduction in oxygen diffusivity in the La-doped systems due to a high degree of oxygen vacancy clustering in the La-doped SrTiO_3 systems as previously discussed by us [22].

To conclude, p- (Na or Ga) and n- (La or Nb) doped SrTiO_3 perovskites are promising mixed ionic/electronic conductors. Computations predict that doping n-doped SrTiO_3 with small amounts of p-type dopants significantly improves the ionic and electronic conductivity. Experimental observations confirm that introducing small amounts of p-type dopants into the lattice promotes reducibility and conductivity; however, the introduction of too large amounts of p-type dopants in an n-doped material reduces the electronic conductivity.

4. Conclusions

We utilized computational and experimental tools to develop a mixed p- and n-type doping strategy to obtain mixed ionic/electronic conductivity in SrTiO_3 based perovskite oxides. First, we performed DFT calculations of various Na- and Nb-doped SrTiO_3 and Na- and La-doped SrTiO_3 systems. In particular, we performed constrained *ab initio* thermodynamic simulations to determine the phase stability and reducibility of doped SrTiO_3 under synthesized and anodic SOFC conditions. Then, we analyzed the DOS of the most dominant structures in the phase diagrams to compute the number of charge carriers per supercell. The calculations reveal that doping 20% n- (La or Nb) doped SrTiO_3 with small amounts of Na (e.g. 10%) enhances the ionic conductivity of the material by creating oxygen vacancies. The electronic conductivity is improved since the hole doping effect is compensated by the presence of oxygen vacancies such that a mixed ionic/electronic conductor is formed. However, increasing the Na concentration further (e.g. 20%) diminishes the electronic conductivity of the material because the concentration of conduction electrons is reduced by excessive electron holes from the Na dopants. These theoretical predictions are confirmed by experimental observations. Experimentally, we find that introducing small amounts of Na in n-doped SrTiO_3 dramatically enhances the total conductivity. In addition to the reasons suggested theoretically, we also observe an improved stability of the materials. From computational predictions and experimental observations we confirm that a mixed p- and n-doping approach is an efficient doping strategy to obtain mixed ionic/electronic conductivity in perovskite oxides; which could be one of the reasons why a large number of elements can be found in most high performance perovskite electrodes for SOFCs. We note that this doping approach is valid independent of p- and n-doping site since either altering the n-type dopant from La (A-site) to Nb (B-site) or changing the p-type dopant from Ga (B-site) to Na (A-site) does not significantly affect the ionic and electronic conductivity of the doped material.

Acknowledgments

This work has been funded by the Heterogeneous Functional Materials Center (HeteroFoaM), an Energy Frontier Research Center

funded by the U.S. Department of Energy, Office of Basic Energy Sciences under Award Number DE-SC0001061. Computations were performed at the U.S. Department of Energy facilities located at EMSL, a national scientific user facility located at Pacific Northwest National Laboratory (Grant Proposal No. 47447) and at the National Energy Research Scientific Computing Center (NERSC). Furthermore, a portion of this research was performed at Teragrid resources provided by the National Institute for Computational Sciences (NICS), Purdue University, and Texas Advanced Computing Center (TACC) under grant number TG-CTS090100. Finally, computing resources from the USC NanoCenter and USC's High Performance Computing Group are gratefully acknowledged.

Appendix A. Supporting information

Supplementary data related to this article can be found at <http://dx.doi.org/10.1016/j.jpowsour.2013.07.040>.

References

- [1] D. Sarantidis, A. Atkinson, *Fuel Cells* 7 (2007) 246–258.
- [2] T. Iwata, *J. Electrochem. Soc.* 143 (1996) 1521–1525.
- [3] A. Tsoga, A. Naoumidis, P. Nikolopoulos, *Acta Mater.* 44 (1996) 3679–3692.
- [4] D. Simionis, F. Tietz, D. Stover, *Solid State Ionics* 132 (2000) 241–251.
- [5] M. Guillodo, P. Vernoux, J. Fouletier, *Solid State Ionics* 127 (2000) 99–107.
- [6] Y.B. Lin, Z.L. Zhan, S.A. Barnett, *J. Power Sources* 158 (2006) 1313–1316.
- [7] R.J. Gorte, J.M. Vohs, *Curr. Opin. Colloid Interface Sci.* 14 (2009) 236–244.
- [8] D. Neagu, J.T.S. Irvine, *Chem. Mater.* 22 (2010) 5042–5053.
- [9] S.W. Tao, J.T.S. Irvine, *Nat. Mater.* 2 (2003) 320–323.
- [10] Y.H. Huang, R.I. Dass, Z.L. Xing, J.B. Goodenough, *Science* 312 (2006) 254–257.
- [11] D.P. Fagg, V.V. Kharton, A.V. Kovalevsky, A.P. Viskup, E.N. Naumovich, J.R. Frade, *J. Eur. Ceram. Soc.* 21 (2001) 1831–1835.
- [12] S.Q. Hui, A. Petric, *J. Eur. Ceram. Soc.* 22 (2002) 1673–1681.
- [13] T. Ishihara, H. Matsuda, Y. Takita, *J. Am. Chem. Soc.* 116 (1994) 3801–3803.
- [14] M. Feng, J.B. Goodenough, *Eur. J. Solid State Inorg. Chem.* 31 (1994) 663–672.
- [15] K.Q. Huang, M. Feng, J.B. Goodenough, M. Schmerling, *J. Electrochem. Soc.* 143 (1996) 3630–3636.
- [16] A. Sin, E. Kopnin, Y. Dubitsky, A. Zaopo, A.S. Arico, L.R. Gullo, D. La Rosa, V. Antonucci, *J. Power Sources* 145 (2005) 68–73.
- [17] P. Vernoux, E. Djurado, M. Guillodo, *J. Am. Ceram. Soc.* 84 (2001) 2289–2295.
- [18] J. Canales-Vazquez, S.W. Tao, J.T.S. Irvine, *Solid State Ionics* 159 (2003) 159–165.
- [19] O.A. Marina, N.L. Canfield, J.W. Stevenson, *Solid State Ionics* 149 (2002) 21–28.
- [20] J. Canales-Vazquez, J.C. Ruiz-Morales, J.T.S. Irvine, W.Z. Zhou, *J. Electrochem. Soc.* 152 (2005) A1458–A1465.
- [21] G. Xiao, X. Dong, K. Huang, F. Chen, *Mater. Res. Bull.* 46 (2011) 57–61.
- [22] S. Suthirakun, S.C. Ammal, G.L. Xiao, F.L. Chen, K.V. Huang, H.C. zur Loyer, A. Heyden, *Solid State Ionics* 228 (2012) 37–45.
- [23] S. Suthirakun, S.C. Ammal, G.L. Xiao, F.L. Chen, H.C. zur Loyer, A. Heyden, *Phys. Rev. B* 84 (2011) 205102.
- [24] D. Neagu, J.T.S. Irvine, *Chem. Mater.* 23 (2011) 1607.
- [25] J.B. Goodenough, Y.H. Huang, *J. Power Sources* 173 (2007) 1–10.
- [26] T. Kolodiaznyi, A. Petric, *J. Electroceram.* 15 (2005) 5–11.
- [27] T. Ishihara, *Perovskite Oxide for Solid Oxide Fuel Cells*, Springer, New York, 2009.
- [28] K. Vidyasagar, A. Reller, J. Gopalakrishnan, C.N.R. Rao, *J. Chem. Soc. Chem. Commun.* (1985) 7–8.
- [29] J.A. Kilner, *Solid State Ionics* 129 (2000) 13–23.
- [30] T. Ishihara, H. Matsuda, M.A. binBustam, Y. Takita, *Solid State Ionics* 86–8 (1996) 197–201.
- [31] P.R. Slater, J.T.S. Irvine, T. Ishihara, Y. Takita, *J. Solid State Chem.* 139 (1998) 135–143.
- [32] M.J. Akhtar, Z.U.N. Akhtar, R.A. Jackson, C.R.A. Catlow, *J. Am. Ceram. Soc.* 78 (1995) 421–428.
- [33] C.H. Park, D.J. Chadi, *Phys. Rev. B* 57 (1998) R13961–R13964.
- [34] H. Donnerberg, A. Birkholz, *J. Phys. Condens. Matter* 12 (2000) 8239–8247.
- [35] M. Tsukada, C. Satoko, H. Adachi, *J. Phys. Soc. Jpn.* 48 (1980) 200–210.
- [36] A. Stashans, F. Vargas, *Mater. Lett.* 50 (2001) 145–148.
- [37] D. Ricci, G. Bano, G. Pacchioni, F. Illas, *Phys. Rev. B* 68 (2003) 224105.
- [38] J.N. Yun, Z.Y. Zhang, J.F. Yan, W. Zhao, *J. Appl. Phys.* 107 (2010) 103711.
- [39] W. Sugimoto, M. Shirata, M. Takemoto, S. Hayami, Y. Sugahara, K. Kuroda, *Solid State Ionics* 108 (1998) 315–319.
- [40] G. Kresse, J. Furthmüller, *Phys. Rev. B* 54 (1996) 11169–11186.
- [41] J.P. Perdew, K. Burke, M. Ernzerhof, *Phys. Rev. Lett.* 77 (1996) 3865–3868.
- [42] G. Kresse, D. Joubert, *Phys. Rev. B* 59 (1999) 1758–1775.
- [43] H.J. Monkhorst, J.D. Pack, *Phys. Rev. B* 13 (1976) 5188–5192.
- [44] Y.A. Abramov, V.G. Tsirelson, V.E. Zavodnik, S.A. Ivanov, I.D. Brown, *Acta Crystallogr. B* 51 (1995) 942–951.

- [45] K. van Benthem, C. Elsasser, R.H. French, *J. Appl. Phys.* 90 (2001) 6156–6164.
- [46] J. Robertson, K. Xiong, S.J. Clark, *Thin Solid Films* 496 (2006) 1–7.
- [47] C. Zhang, C.L. Wang, J.C. Li, K. Yang, Y.F. Zhang, Q.Z. Wu, *Mater. Chem. Phys.* 107 (2008) 215–219.
- [48] G. Hautier, S.P. Ong, A. Jain, C.J. Moore, G. Ceder, *Phys. Rev. B* 85 (2012) 155208.
- [49] S.C. Ammal, A. Heyden, *J. Chem. Phys.* 133 (2010) 164703.
- [50] J.K. Norskov, J. Rossmeisl, A. Logadottir, L. Lindqvist, J.R. Kitchin, T. Bligaard, H. Jonsson, *J. Phys. Chem. B* 108 (2004) 17886–17892.
- [51] P.W. Atkins, *Physical Chemistry*, sixth ed., Oxford University Press, Oxford, 1998.
- [52] S. Ohta, T. Nomura, H. Ohta, K. Koumoto, *J. Appl. Phys.* 97 (2005) 034106.
- [53] S. Laursen, S. Linic, *Phys. Chem. Chem. Phys.* 11 (2009) 11006–11012.
- [54] S. Laursen, S. Linic, *J. Phys. Chem. C* 113 (2009) 6689–6693.
- [55] J. Rogal, K. Reuter, M. Scheffler, *Phys. Rev. B* 75 (2007) 205433.
- [56] Q.L. Ma, F. Tietz, D. Stover, *Solid State Ionics* 192 (2011) 535–539.
- [57] N.F. Mott, *Rev. Mod. Phys.* 40 (1968) 677.